Electrochimica Acta 525 (2025) 146159

Contents lists available at ScienceDirect

Electrochimica Acta

journal homepage: www.journals.elsevier.com/electrochimica-acta

Chemical and electrochemical surface treatments to grow magnesium hydroxystannate/manganese stearate coating for tuning biodegradation rate of AZ31 for bioresorbable implants

V. Verro [a], F. Di Franco [a], F. Carfì Pavia [a], F. La Monica [b], M. Santamaria [a,*]

[a] Dipartimento di Ingegneria, Università di Palermo, Palermo, Italy
[b] Dipartimento di Scienze e Tecnologie Biologiche Chimiche e Farmaceutiche, Università di Palermo, Palermo, Italy

ARTICLE INFO

Keywords:
Magnesium alloys
Biomedical
Superhydrophobic coating
Electrodeposition
Stearate
Hydrogen evolution
DMEM

ABSTRACT

A double layered coating was deposited on AZ31 to tune biodegradation rate of this alloy in physiological solution at 37°C. A first chemical conversion process in a stannate ions containing alkaline solution was carried out on AZ31 to induce the growth of a $MgSn(OH)_6$ layer constituted by closely packed spheres. A manganese stearate ($Mn[CH_3(CH_2)_{16}COO]_2$) layer was electrodeposited on the magnesium hydroxystannate to make the surface of the alloy hydrophobic. The resulting coating allowed to increase the corrosion resistance in Dulbecco's Modified Eagle Medium (DMEM) at 37°C, as assessed by recording polarization curves and electrochemical impedance spectra. Hydrogen evolution rate in DMEM, directly measured using gas chromatography to avoid misleading information due to negative difference effect, was reduced by the coating since the early stage of immersion. According to cytotoxicity tests with MC3T3 pre-osteoblastic cells, the coating resulted biocompatible.

1. Introduction

Metallic materials are widely used for biomedical applications, as repair or replacement materials of the diseased or damaged bone tissue. Compared with traditionally employed stainless steels, titanium alloys and chromium-cobalt based alloys, magnesium and its alloys show special mechanical and chemical properties. Indeed, Mg alloys have a low density (1.74 - 2.0 g cm^{-3}) and an elastic modulus between 41 and 45 GPa, very well matching with that of natural bone. Moreover, Mg ions released by these alloys as a consequence of corrosion as well as wear processes are not harmful to the body [1–5]. Therefore, magnesium and its alloys are promising candidate materials for biodegradable implants for orthopaedic applications and vascular stents [6–9].

However, due to the very low reduction potential and to the poor corrosion resistance in chloride containing environments (as human body fluids or blood plasma), the degradation rate of magnesium and its alloys is so high that the mechanical integrity before the diseased or damaged bone tissue healed is not always maintained [10,11]. Moreover, since water reduction is the common cathodic process during corrosion of Mg and its alloys, the high corrosion rate implies a high H_2 evolution rate. An overabundant hydrogen formation may lead to detrimental gas pockets around the implant, and it may also cause alkalization in the vicinity of the corroding surface, discussed as possibly being deleterious for the surrounding biological environment [12–14].

The simplest way to slow down corrosion is to form a coating on the magnesium substrate to provide a barrier toward the contact between the substrate and the environments. There are many coating technologies which can be used to coat the magnesium substrate, such as electrochemical plating, chemical conversion coating, physical vapour deposition, laser surface treatment and anodic oxidation [15–22]. Among these technologies the latter is one of the most effective and employed processes, even if the growth of protective anodic layers on Mg and Mg alloys is difficult due to the unfavourable Pilling-Bedworth ratio [23–29]. The latter is defined as the ratio of the volume of the elementary cell of a metal oxide to the volume of the elementary cell of the corresponding metal oxidized to produce the oxide, that is 0.8 for MgO. This would cause the formation of a porous and/or cracked and thus unprotective layer. Chemical conversion treatments are easy to apply and cost-effective, since they are electroless processes generally carried out in mild conditions (moderate temperature and atmospheric pressure). However, the composition of the conversion bath must be properly selected to avoid the formation of compounds detrimental for human body, thus excluding the possibility to use surface treatments relying on chromates, which are very effective in corrosion inhibition

* Corresponding author.
E-mail address: monica.santamaria@unipa.it (M. Santamaria).

https://doi.org/10.1016/j.electacta.2025.146159
Received 7 January 2025; Received in revised form 5 March 2025; Accepted 30 March 2025
Available online 31 March 2025

Table 1
Samples treatment summary and names used in the paper.

sample name	I step: Conversion coating	II step: Hydrophobic coating
AZ31	-	-
AZ31/CC30	30 min	-
AZ31/CC60	60 min	-
AZ31/MnST	-	0.5 C cm^{-2}
AZ31/CC30/MnST	30 min	0.5 C cm^{-2}

Table 2
DMEM solution composition.

substance	[mg L^{-1}]	substance	[mg L^{-1}]	substance	[mg L^{-1}]
NaCl	6400	L-Cysteine	48	L-Valine	94
KCl	400	L-Glutamine	580	Glycine	30
$CaCl_2$	200	L-Histidine HCl	42	L-Serine	42
$MgSO_4$ $7H_2O$	200	L-Isoleucine	106	Cholinchloride	4
Na_2HPO_4	124	L-Leucine	106	Folic acid	4
D-Glucose	1000	L-Lysine HCl	146	Myo-Inositol	7.2
$Fe(NO_3)_3$ H_2O	0.1	L-Methionine	30	Nicotinamide	4
Na-Pyruvate	110	L-Phenylanine	66	Da-Ca-Pantothenate	4
Phenol red	15	L-Threonine	95	Pyridoxal HCl	4
$NaHCO_3$	3700	L-Tryptophan	16	Riboflavin	0.4
L-Arginine HCl	84	L-Tyrosine	72	Thiamine-HCl	4

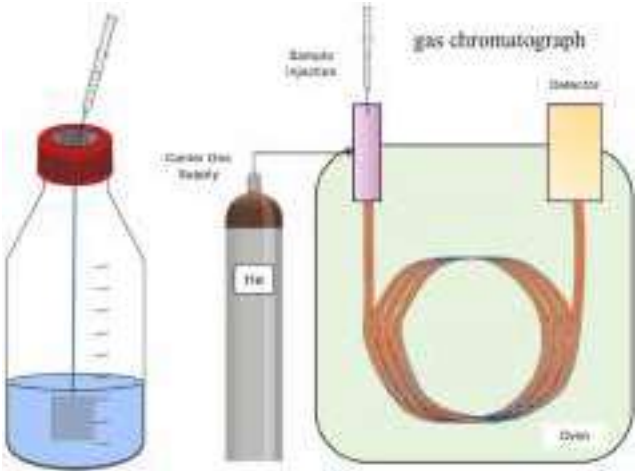

Fig. 1. Setup used for the direct estimation of hydrogen evolution rate.

but are toxic and carcinogenic [30–32]. Stannate conversion coatings are a good alternative to chromate coatings although they provide less corrosion resistance to Mg alloys [33–37]. On the other hand, another promising method to grow corrosion resistant coating is the electroplating, a process traditionally used for the deposition of metallic layers but that can be also used to induce the formation of functional hydrophobic coating preventing corrosion and biofouling [38–41]. However, they suffer adhesion problems with a strong impact on their durability.

In the present work, we propose a new strategy to grow an efficient coating able to tune the biodegradation rate of AZ31 alloy by carrying out a two-step process, i.e. chemical conversion in a stannate containing aqueous solution followed by the electrodeposition of a functional hydrophobic layer of manganese stearate in the attempt to reduce the corrosion rate of metallic surfaces by preventing corrosive environment from reaching the surface. The presence of a textured conversion coating

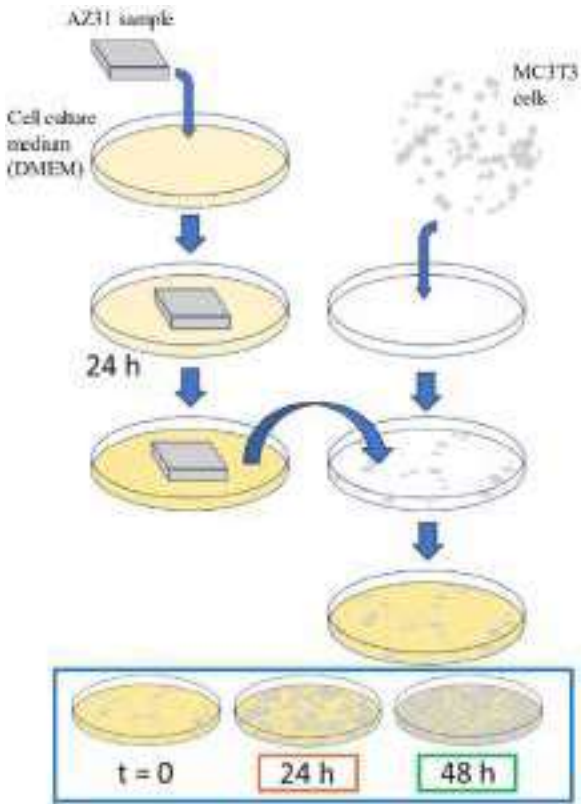

Fig. 2. Viability assay: experimental setup.

will improve the adhesion of the hydrophobic layer with consequent beneficial effect on its stability. Structure, morphology and composition of the coatings will be studied by X-ray diffraction, Scanning Electron Microscopy and FT-IR, while their corrosion resistance will be assessed recording polarization curves and electrochemical impedance spectra in Dulbecco's Modified Eagle Medium (DMEM) solution. To avoid misleading estimates due to negative difference effect [42–46], direct measurements of hydrogen evolution rate will be carried out by following the concentration of evolved H_2 in the environment by gas chromatography, while cytocompatibility tests will allow to assess the biocompatibility of the coated alloys.

2. Materials and methods

2.1. Preparation of samples

AZ31 Mg alloy (Mg 96 %, Al 3 %, Zn 1 %, Goodfellow) 20 × 20 mm coupons were cut and mechanically grinded with silicon carbide grinding papers (Buehler) up to P2500 grit, while quenching in ethanol ($C_2H_6O \geq 99.5$ % - Emplura). Then, samples were ultrasonically cleaned in ethanol for 10 min and dried at room temperature.

2.2. Chemical conversion coating

Tin based conversion coating was obtained by immersion of samples in a water-based solution containing 9.95 g/L sodium hydroxide (NaOH - Fluka), 49.87 g/L potassium stannate (K_2SnO_2 $3H_2O$ - Thermo-Scientific), 9.95 g/L sodium acetate ($NaC_2H_3O_2$ $3H_2O$ - Carlo Erba Reagents), 49.87 g/L sodium pyrophosphate tetrabasic ($Na_4P_2O_7$ - Sigma-Aldrich) [47]. During the conversion process, temperature was controlled and maintained at 82 ± 5 °C, without stirring. Different immersion time were investigated (30 and 60 min). After immersion, converted samples were rinsed in DI water and dried at room temperature. Open circuit potential (OCP) was recorded over time during the

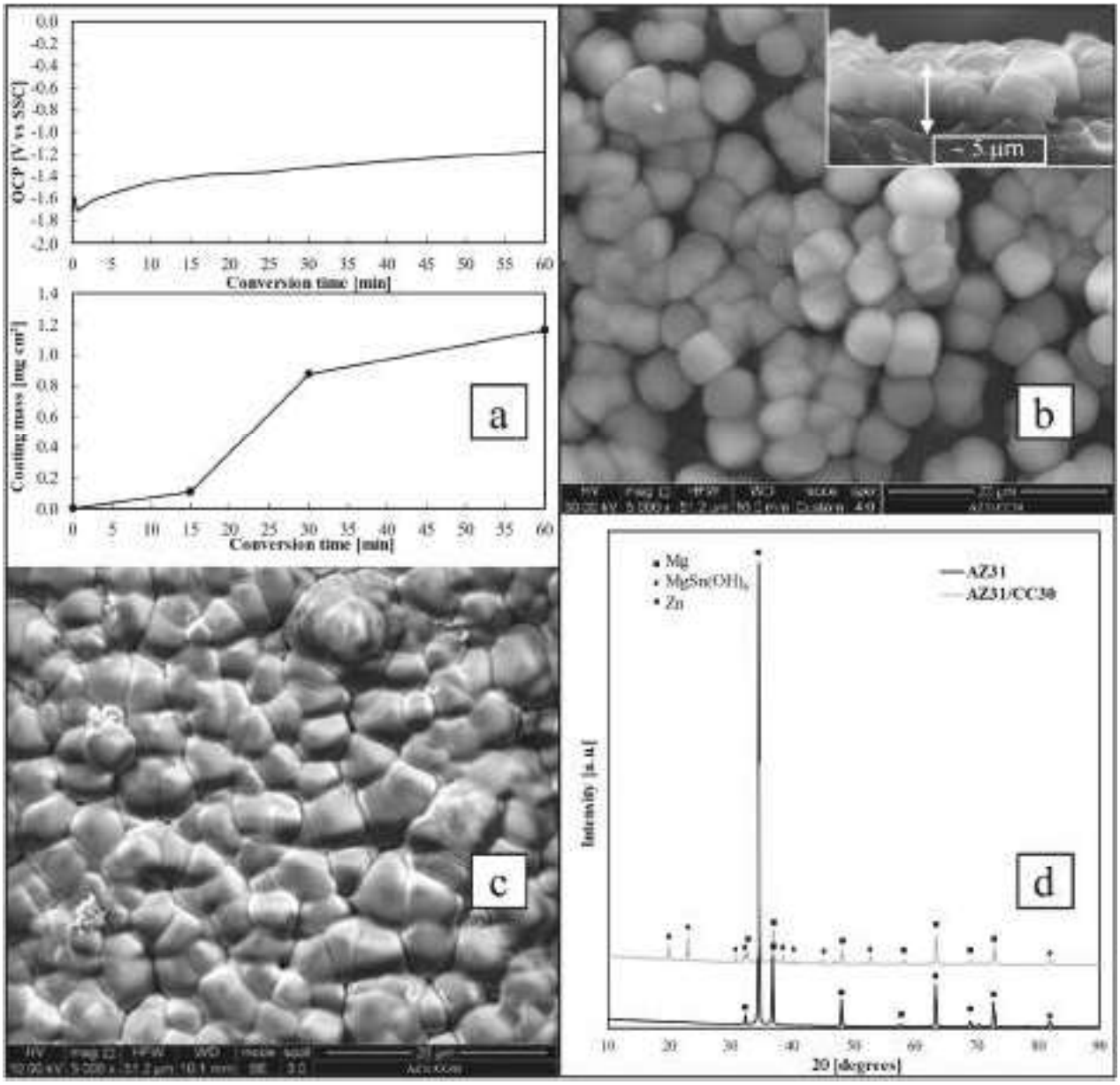

Fig. 3. a) Open circuit potential recorded during chemical conversion (up) and conversion coating mass gain at different immersion time (down). b) SEM image of conversion coating after 30 min and coating cross-section (inset). c) SEM image of conversion coating after 60 min. d) XRD spectra of bare AZ31 and sample with conversion coating.

Table 3
EDX analysis of the coated samples.

At.%	O	C	Mg	Sn	Mn
AZ31/CC30	74.97		10.50	14.53	
AZ31/CC60	74.46		11.85	13.69	
AZ31/MnST	2.34	77.85	19.49		0.32
AZ31/CC30/MnST	60.48	10.32	19.52	9.08	0.60

chemical conversion process by using a three-electrode cell configuration with Ag/AgCl/sat. KCl as a reference electrode (0.197 V vs SHE), and a Pt mesh as counter electrode. Gravimetric experiments were carried out in order to measure mass gain due to the stannate based conversion coating. For each immersion time the mean value between at least 5 samples was calculated.

2.3. Hydrophobic coating

Electrodeposition process was carried out in ethanol (C_2H_6O ≥99.5 % - Emplura), with 0.1 M stearic acid ($CH_3(CH_2)_{16}COOH$ - Sigma-Aldrich) and 0.05 M manganese chloride ($MnCl_2$ $4H_2O$ - Carlo Erba Reagents). The solution was prepared at 50 °C, such temperature was maintained during the process and samples were immersed for 15 min prior to the beginning of the deposition. A two-electrode configuration was adopted, imposing a range of different potentials between cathode (AZ31 sample) and anode (two rectangular sheet of carbon paper): potentials in the range −5 V / −20 V were investigated. Samples were then rinsed in ethanol and dried at room temperature for 24h. The degradation of the obtained coating was assessed estimating Mn and Sn release after immersion in testing solution for 24 h, using a PerkinElmer Optima 2100 DV. ICP-OES analyses were performed on solutions diluted 1:10 with 2 wt. % nitric acid (65 % Suprapur, Sigma-Aldrich) aqueous solution.

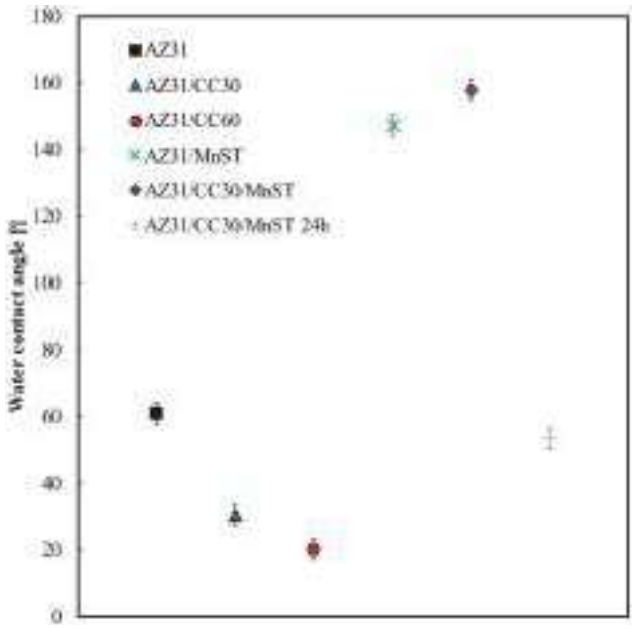

Fig. 4. Contact angle measurements.

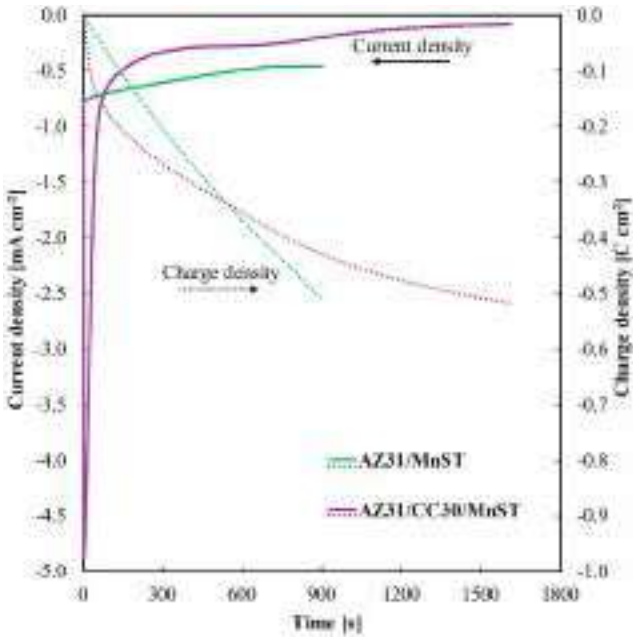

Fig. 5. Stearate deposition curves obtained on AZ31 bare and on AZ31/CC30 substrate samples.

The procedures each sample has undergone are reported in Table 1.

2.4. Electrochemical characterization

Bare AZ31 and coated samples were studied by means of OCP measurement over time, EIS spectra and polarization curves, using a three-electrode configuration and Ag/AgCl/sat. KCl as a reference electrode (0.197 V vs SHE), while a high specific area Pt mesh was adopted as counter electrode. OCP measurements were recorded for 30 min, EIS spectra were measured with ± 10 mV oscillations with respect to the OCP for frequencies in the range 10 mHz / 100 KHz. Polarization curves were scanned in the potential range between −0.15 V vs OCP and −0.50 V vs SSC at 5 mV s^{-1}. Each electrochemical measurement was performed using a ParStat 2273 potentiostat. Testing solution was Dulbecco's Modified Eagle Medium (DMEM with stable Glutamine, with 1.0 g l^{-1} Glucose - Genaxxon bioscience), maintained at 37 °C in order to mimic physiological environment (composition reported in Table 2 [2]).

2.5. Surface analysis

Surface morphologies of bare and coated samples were investigated with SEM (FEI Quanta 200 FEG SEM instrument) images and EDX spectroscopy. FT-IR analysis was also carried out, using a FT-IR/NI Spectrum 400 spectrophotometer (Perkin Elmer, Waltham, MA, U.S. A.), in the range 4000–450 cm^{-1}. X-ray diffraction (XRD) spectra were collected in the angle range 2θ = 10° - 90°, using a PanAlytical Empyrean diffractometer with a Cu anode (Cu Kα radiation, λ = 0.15405 nm) equipped with a PIXCel1D detector (voltage: 40 kV, current: 40 mA). Contact angle measurements were carried out with an FTA 1000 instrument, with 5 μl drops of DI water and acquiring pictures with a blue led backlight in order to have optimal contrast; each sample was tested at least in 3 different position and the mean value was considered.

2.6. H_2 evolution measurements

In order to directly measure hydrogen evolution, each sample was immersed in a bottle containing DMEM solution, closed with a bromobutyl rubber stopper. Bottles were kept at 37° in an incubator, the rubber stoppers were pierced with the needle of a 500 μl Hamilton gastight syringe in order to collect a gas sample. Solution volume/immersed area ratio for each sample was 25 ml cm^{-2}, with 950 ml head volume in the bottle. Gas samples were collected periodically and analysed with a HP 6890 Series gas chromatograph (Fig. 1).

2.7. Cytotoxicity tests

The AZ31, AZ31/CC30, and AZ31/CC30MnST samples were sterilized by incubation in 70 % ethanol for 24 h, followed by a UV treatment for 2 h (1 hour per side) in a laminar flow hood. They were then placed into a petri dish and treated with complete medium, composed of DMEM high glucose (Sigma-Aldrich), 10 % Fetal Bovine Serum (FBS), 100 μg/ml Penicillin/Streptomycin (Sigma-Aldrich), and 2 mM L-glutamine, with a surface/volume ratio of 3 cm^2 ml^{-1}. After 24 h of incubation, the medium was used to treat cells. Specifically, $7 \bullet 10^3$ MC3T3 pre-osteoblastic cells were cultured in a 96-well plate with 150 μl of complete medium. After 24 h, the medium was replaced with the conditioned medium derived from the samples or with the normal medium (as a positive control named CTRL). After 24- and 48-hours cell viability was assessed using Alamar Blue cell viability reagent (Thermo-Scientific), which is based on resazurin. Essentially, live cells metabolize resazurin into resorufin, which displays intrinsic fluorescence. The medium was replaced with 100 μl of the reagent diluted 1:10 with a complete medium. Cells were incubated for 2 h at 37 °C in a humidified incubator with 5 % CO_2. Fluorescence intensity, directly correlated with cell viability, was measured using a plate reader (BioTek Sinergy HT) at an emission wavelength of 530/25 nm and an emission peak at 590/35 nm. A schematic representation of the experimental setup is shown in Fig. 2.

3. Results and discussion

3.1. Chemical conversion coating

AZ31 coupons were immersed in the conversion bath (T = 82 °C) to induce the growth of hydroxystannate layer on their surface, according to the following reactions:

$$Mg \rightarrow Mg^{2+} + 2e^- \quad (1)$$

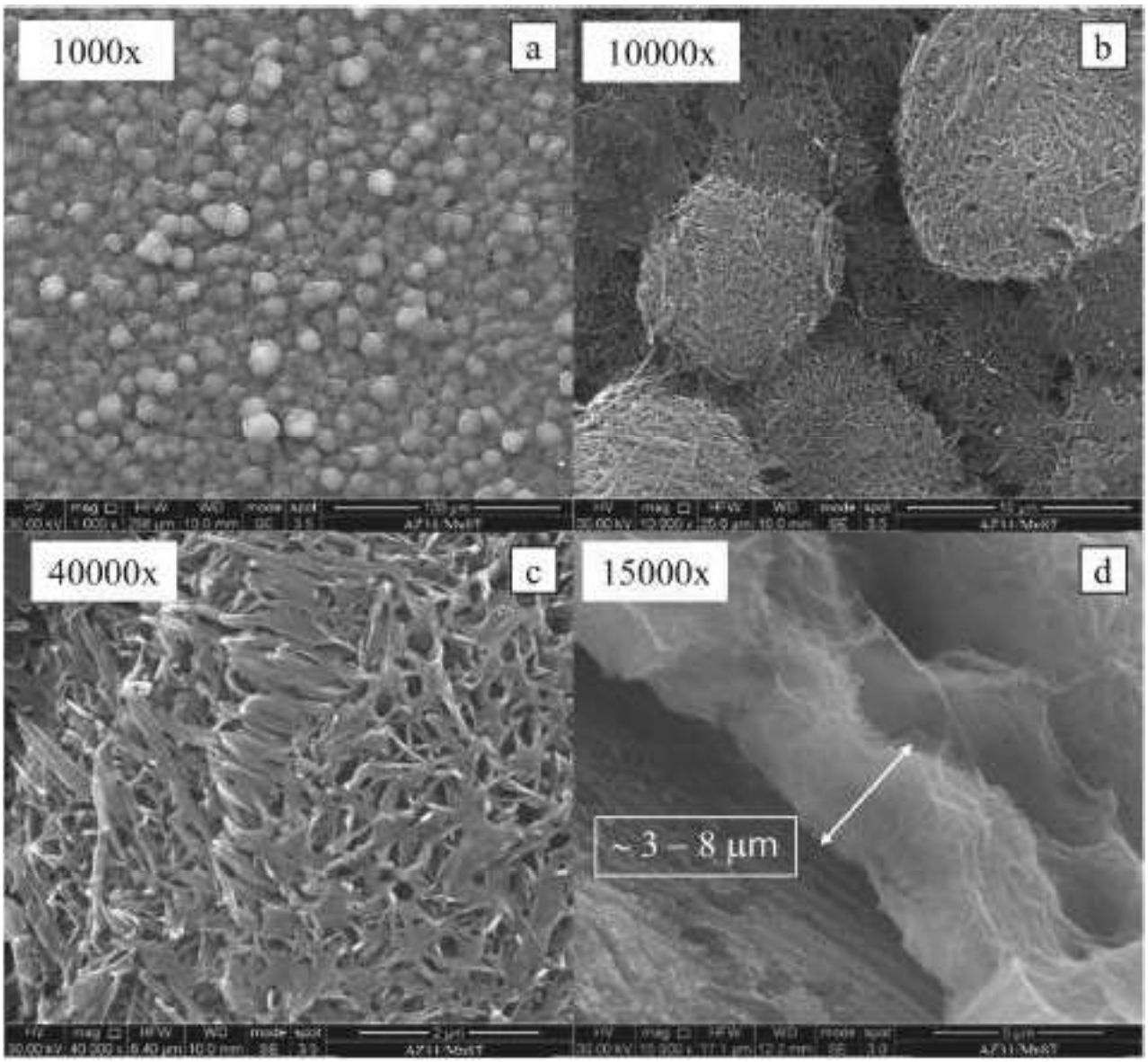

Fig. 6. a, b, c) SEM images of AZ31/MnST at different magnification. d) MnST coating cross section.

$$2H_2O + 2e^- \rightarrow H_2 + 2OH^- \quad (2)$$

$$Mg^{2+} + SnO_3{}^{2-} + 3H_2O \rightarrow MgSn(OH)_6\downarrow \quad (3)$$

Indeed, due to its very low equilibrium reduction potential, magnesium is oxidized by water with simultaneous release of Mg^{2+} and OH^- ions and consequent $MgSn(OH)_6$ precipitation. The conversion process was followed as a function of time with a specific focus on open circuit potential and mass gain (see Fig. 3a).

OCP raises during conversion in agreement with the formation of a protective coating and reduction of bare magnesium alloy surface exposed to the conversion bath and, simultaneously, the total mass increases due to the formation of the coating. SEM analysis of the surface of samples AZ31/CC30 and AZ31/CC60 discloses the formation of a coating constituted by closely packed spheres that according to the EDX analysis contain Mg, Sn and O (see Table 3).

Notably, the longer is the conversion time the higher is the coverage degree (see Figs. 3b and 3c). After the growth of the coating some sample was bended and partially scratched in order to measure the thickness of conversion coating, that was estimated to be ~5 µm (see inset in Fig. 3b). XRD diffraction pattern for coated alloys revealed the presence of reflections attributed to crystalline $MgSn(OH)_6$ (see Fig. 3d) confirming the successful formation of magnesium hydroxystannate layer. The chemical conversion (i.e. the growth of $MgSn(OH)_6$) makes the surface strongly hydrophilic, showing contact angles lower than 30° (Fig. 4).

3.2. Hydrophobic coating

A second electrochemical deposition step was carried out on converted alloys to further improve their corrosion resistance in the attempt to seal the remaining exposed metal surface with a hydrophobic compound. Therefore, magnesium alloys after the growth on its surfaces of $MgSn(OH)_6$ by conversion coating process were immersed in a fatty acid (stearic acid) and manganese salt containing ethanol solution, and they were cathodically polarized (at -10 V) to induce the precipitation of manganese stearate according to the following reactions:

$$CH_3(CH_2)_{16}COOH \underset{\rightarrow}{\leftarrow} CH_3(CH_2)_{16}COO^- + H^+ \quad (4)$$

$$2H_2O + 2e^- \rightarrow H_2 + 2OH^- \quad (5)$$

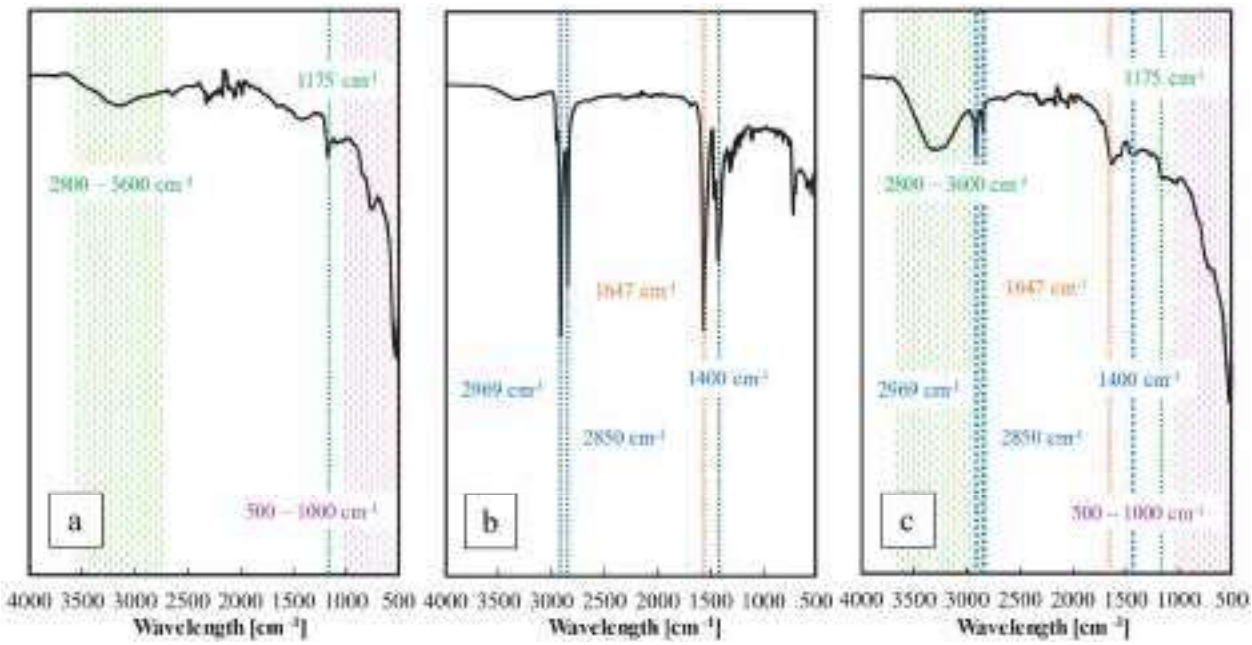

Fig. 7. FT-IR spectra for AZ31 samples with: a) conversion coating (AZ31/CC30); b) hydrophobic coating on bare substrate (AZ31/MnST); c) hydrophobic coating on 30 min conversion coating (AZ31/CC30/MnST).

$$Mn^{2+} + 2CH_3(CH_2)_{16}COO^- \rightarrow Mn[CH_3(CH_2)_{16}COO]_2\downarrow \quad (6)$$

For matter of comparison, this electrodeposition step was also carried out on bare AZ31 to highlight the role of the conversion coating on the corrosion rate of the samples. Fig. 5 shows the current density transients recorded for both bare and converted alloy. In both cases the absolute value of the current density decreases as a function of time suggesting that the deposited layer covers the metallic surface. The process was stopped after the circulation of ~ 0.5 C cm^{-2}.

The successful deposition of manganese stearate on AZ31 was confirmed by analysing the morphology of the coating soon after electrodeposition by SEM and by analysing surfaces composition by EDX and FTIR. Figs. 6a and 6b show the surface morphology of stearate manganese deposited on bare AZ31, constituted by quasi-spherical structures with smaller spiky extremities (see Fig. 6c), that cause a great increase in specific surface area. EDX analysis reveals a high carbon content and the presence of manganese. From the cross section of Fig. 6d, the coating appears to be constituted by spherical structures embedded in a flat MnST layer, with a thickness ranging between 3 and 8 μm.

FT-IR spectra for this coating (Fig. 7b) reveal absorption bands in the range 2850-2969 cm^{-1} that can be attributed to C-H group symmetric and asymmetric vibration, and another peak at 1400 cm^{-1} related to C-H bending. A peak at 1647 cm^{-1} can be attributed to COO-, due to the formation of the stearate salt [48]. The contact angles on such coating showed a transition to the hydrophobic behaviour, with measured angles of ~ 147°. It is important to mention that stearate coating electrodeposited on bare samples appears to have a poor adhesion since it can be easily detached releasing powder.

A different morphology is shown by coating on AZ31 after 30 minutes of chemical conversion (see Fig. 8). In this latter case manganese stearate seems to wrap the existing magnesium hydroxystannate spheres, generating a very rough layer covering all the spheres. Notably, manganese stearate seal the space among the $MgSn(OH)_6$ spheres (compare Fig. 3b with Fig. 8b), thus inhibiting the contact between the alloy and the aggressive environment. By analysing the surface of cracked coated samples, it was possible to estimate the MnST layer thickness on top of the conversion coating, that resulted to be ~ 10 - 30 nm (see Fig. 8d). EDX analysis confirmed the presence of C and Mn, but also the signal arising from Mg and Sn beneath. FT-IR spectra for the samples with complete coating (Fig. 7c) show the peaks related to the stearate (C-H and COO-), and in addition other bands and peaks related to the conversion coating substrate: a wide absorption band in the range 2800-3600 cm^{-1} and a peak at 1175 cm^{-1} are related to O-H stretching and lattice modes respectively; Mg-O and Sn-O stretching show absorption bands in 500-1000 cm^{-1} range [49]. The measured contact angles on such coating resulted to be > 150°, revealing a superhydrophobic behaviour.

For both AZ31/MnST and AZ31/CC30/MnST the increased specific surface area with a hierarchical structure as well as the low surface free energy characteristic of manganese stearate (24.5 mJ m^{-2} as reported in [50]) explain the high contact angles, greatly reducing the wettability and thus improving corrosion resistance. Indeed, in agreement with the Cassie-Baxter model, the contact angle (θ_R) on a rough surface can be determined by the corresponding static angle (θ) on a flat surface, as expressed in the following equation:

$$cos\theta_R = f_S\ (cos\theta + 1) - 1 \quad (7)$$

with f_s denoting the fraction of the surface effectively in contact with the liquid. By using $\theta = 101^\circ$ for Mn stearate, as reported in [50], the values of $f_s = 0.20$ and $f_s = 0.09$ for AZ31/MnST and AZ31/CC30/MnST respectively were calculated.

However, after 24 h of immersion in DMEM solution, the contact angle decreases to 53° (see Fig. 4) suggesting that the coating loses its superhydrophobicity thus allowing to not repel cells. Indeed, during immersion in the physiological environment, the stearate layer slowly dissolves exposing the beneath $MgSn(OH)_6$ spheres. This finding is confirmed by ICP measurements (see Fig. 9a), revealing that Mn ions are released from stearate hydrophobic coating (~ 1 μg cm^{-2} after 24 hours), while no Sn ions were detected suggesting that $MgSn(OH)_6$ is stable. This is also confirmed by SEM micrographs of the coating after 24 hours of immersion in DMEM solution. The degradation of hydrophobic coating occurs by losing both stearates that fill the space among the $MgSn(OH)_6$ spheres (see Fig. 9b) and stearates covering the surface on the same spheres (see Fig. 9c).

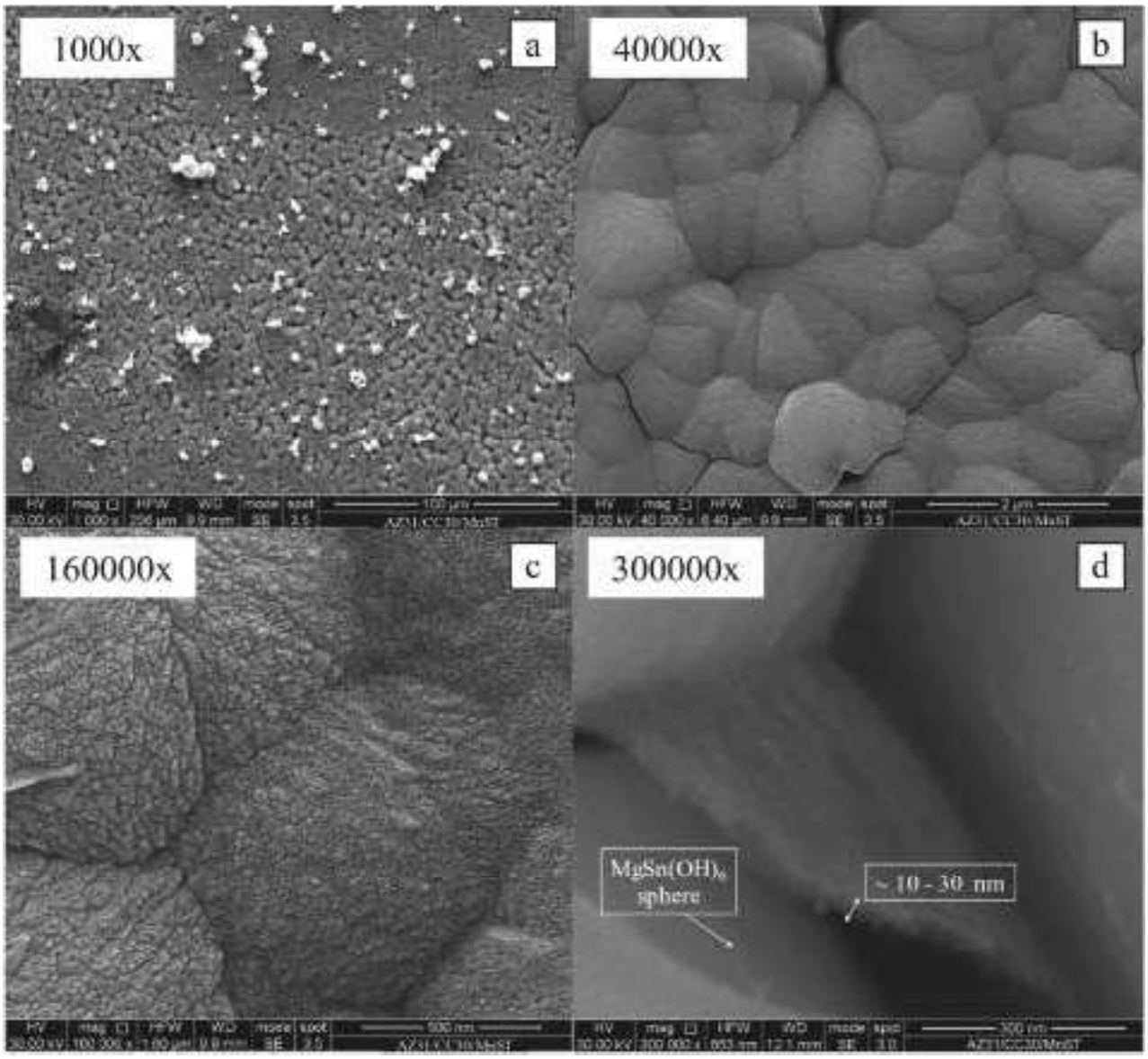

Fig. 8. SEM images of AZ31/CC30/MnST at different magnification. d) Magnification of the cracked MnST coating.

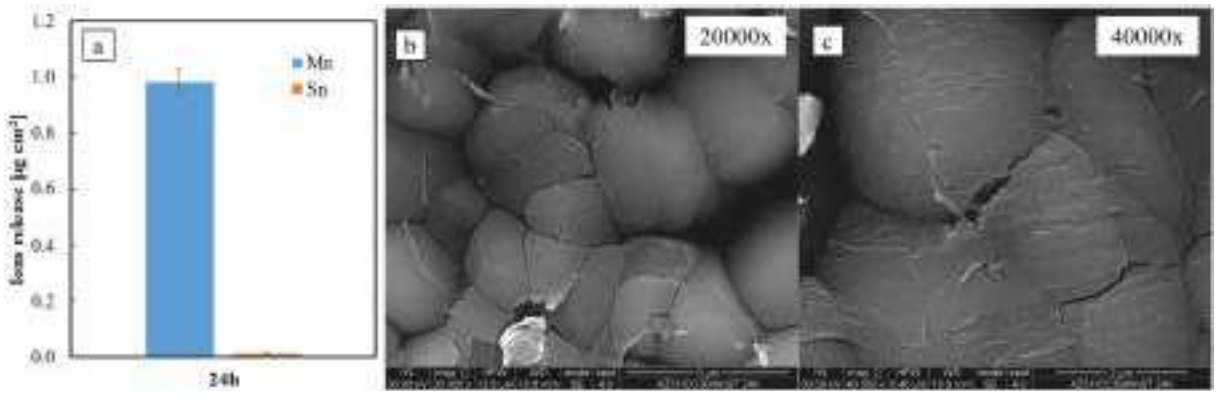

Fig. 9. a) ICP-OES measurements. b, c) SEM micrographs of degraded coating after 24 h of immersion in DMEM.

3.3. Corrosion resistance

Electrochemical characterization of not coated and coated AZ31 was carried out in DMEM solution at 37 °C in order to evaluate corrosion resistance in a physiologic-simulating environment. The uncoated and coated AZ31 alloys were left for 30 min at 37 °C at the open circuit

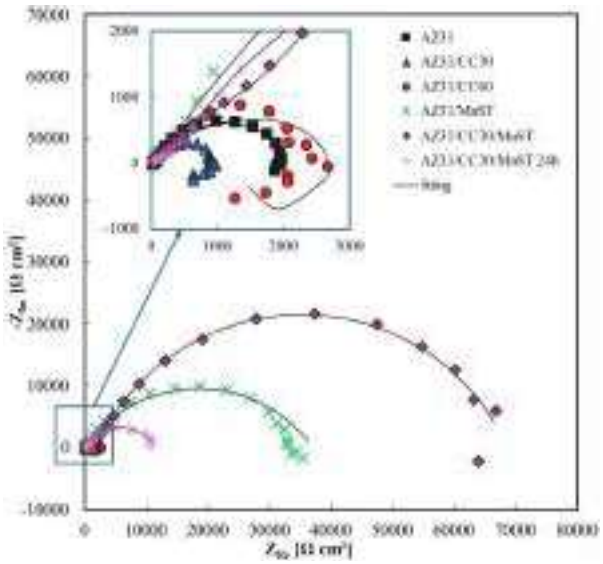

Fig. 10. Nyquist representation of EIS spectra recorded at the open circuit potential in DMEM.

potential (see Fig. 12). The latter resulted to be below the equilibrium potential for hydrogen evolution reaction at pH 7, thus suggesting that the cathodic processes coupled to magnesium oxidation were both oxygen reduction and hydrogen evolution. EIS spectra in the Nyquist representation recorded at open circuit potential are reported in Fig. 10.

For bare AZ31 and AZ31 after 30 and 60 min of chemical conversion, a low frequency inductive loop is present associated to a strong hydrogen evolution and, thus, to a high corrosion rate [51]. Notably, for short conversion time the overall impedance is even lower than that measured for $MgSn(OH)_6$ free sample. Indeed, the uncoated parts of the alloy are prone to localized corrosion, and this explains why the corrosion resistance of this sample is even worse than that of bare alloy.

Conversely, as soon as manganese stearate grows on the surface of the samples and in agreement with the higher water contact angles, the inductive loop disappears and the overall impedance raises significantly. AZ31/MnST samples show a higher impedance than bare AZ31 and the alloys with conversion coating, without the presence of inductive loop at the lower frequencies in the Nyquist plot. The overall impedance of the hydrophobic coating on the bare samples is lower than that of the coating grown on conversion coating, probably because of the worse adhesion on the substrate. However, the coating on the bare samples is compact and adherent enough to reduce considerably the exposed metal surface, thus the absence of the inductive loop.

Samples with the complete hydrophobic coating grown on the stannate based substrate (AZ31/CC30/MnST) show the highest overall impedance, being almost 35 times higher than bare AZ31, and such impedance is maintained at the same order of magnitude even after 24 h of immersion in DMEM. From these results it appears that the morphology obtained with 30 min of immersion in the conversion bath plays an important role in the proper interlocking of the hydrophobic electrodeposited coating.

To get quantitative information from impedance measurements, the EIS spectra were fitted according to the equivalent circuits reported in Fig. 11. For MnST free samples it was necessary to use the equivalent circuit of Fig. 11a, where R_{el} is the electrolyte resistance, Q_{dl} is a constant phase element (CPE) modelling the not ideal behaviour of the double layer capacitance, R_T accounts for the charge transfer kinetic of both half-cell reactions on coated and uncoated regions of the alloy, while the L-R_i series accounts for superfluous hydrogen evolution [51]. The fitting parameters are reported in Table 4. R_T in order of 10^3 Ω cm^2

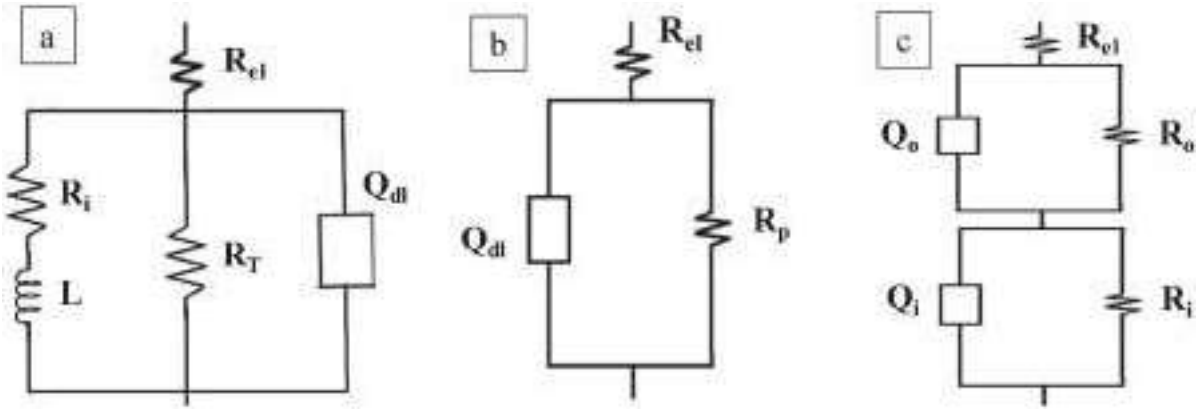

Fig. 11. Equivalent electric circuits adopted to model EIS spectra of the samples.

Table 4
Fitting parameters of the equivalent electric circuits used to model EIS spectra.

	R_{el} [Ω cm^2]	Q_{dl} [S s^n cm^{-2}]	n	R_T [Ω cm^2]	R_i [Ω cm^2]	L [H cm^2]		χ^2	OCP [V vs SSC]
AZ31	30	6.6E-05	0.63	2.2E+03	1.2E+04	2.2E+04		1.4E-02	−1.71
CC30	30	3.4E-05	0.69	9.3E+02	9.7E+02	1.6E+04		1.7E-02	−1.43
CC60	30	7.5E-05	0.52	3.1E+03	2.4E+03	2.2E+04		2.3E-02	−1.43
	R_{el} [Ω cm^2]	**R_p [Ω cm^2]**	**Q_{dl} [S s^n cm^{-2}]**	**n**				**χ^2**	**OCP [V vs SSC]**
AZ31/MnST	30	3.7E+04	4.9E-06	0.60				2.2E-02	−1.65
	R_{el} [Ω cm^2]	**R_o [Ω cm^2]**	**Q_o [S s^n cm^{-2}]**	**n**	**R_i [Ω cm^2]**	**Q_i [S s^n cm^{-2}]**	**n**	**χ^2**	**OCP [V vs SSC]**
AZ31/CC30/MnST	30	2.0E3	7.2E-6	0.58	6.7E4	8.2E-6	0.73	3.4E-3	−1.52
AZ31/CC30/MnST 24h	30	2.5E2	6.6E-6	0.66	1.1E4	3.0E-5	0.67	3.4E-3	−1.44

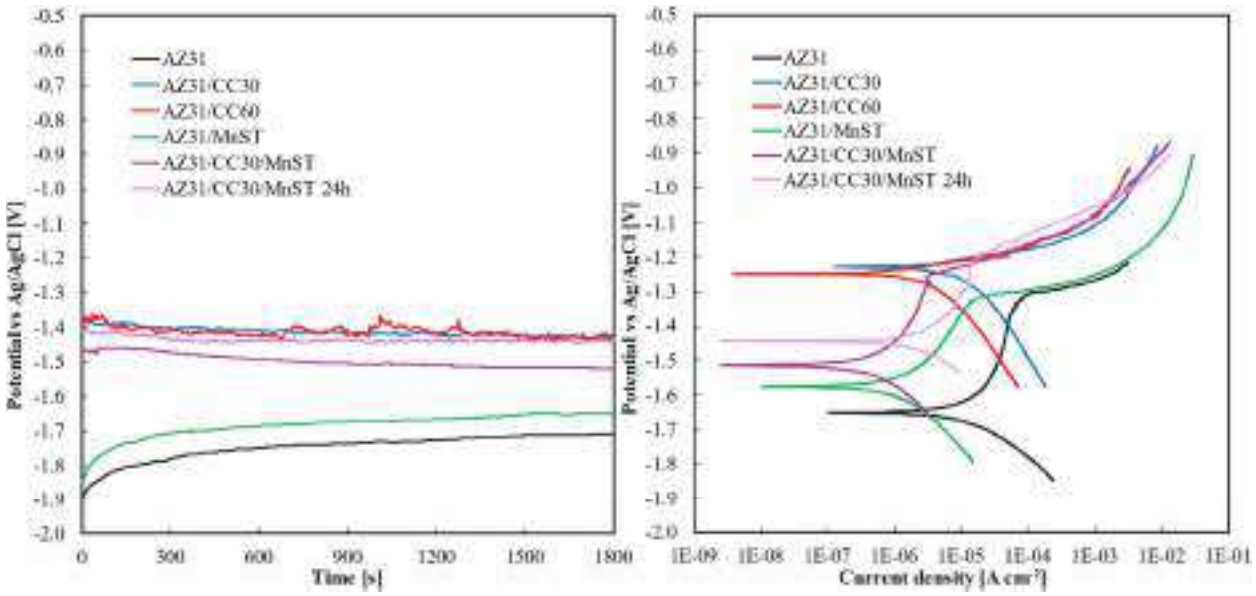

Fig. 12. Open circuit potential of samples (left) and polarization curves (right) in DMEM solution.

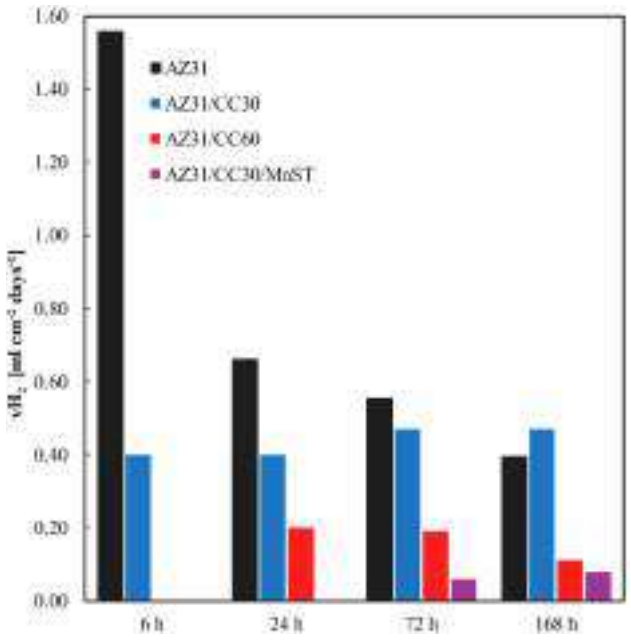

Fig. 13. Direct estimate of hydrogen evolution rate during 168 h.

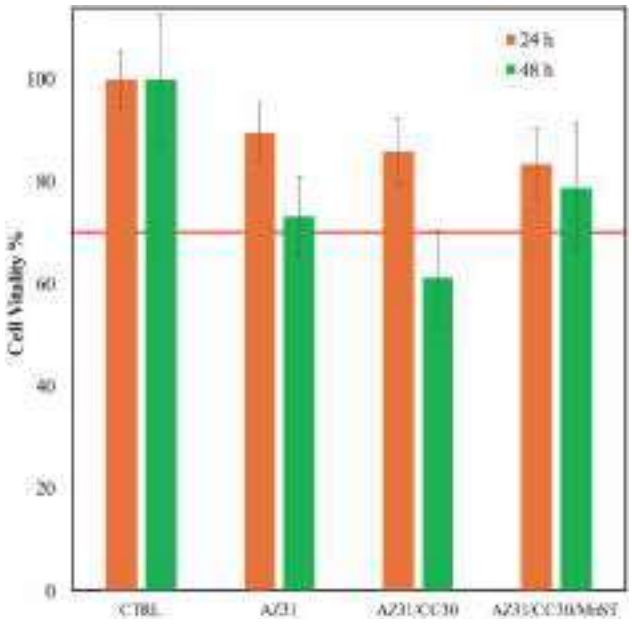

Fig. 14. Cell viability after 24 and 48 h of treatment with normal medium (CTRL) or with AZ31, AZ31/CC30, and AZ31/CC30/MnST conditioned medium.

and L in the order of 10^4 H cm^2 are in agreement with results reported in previous work taking into account the chloride ion concentration [51].

For MnST coated bare AZ31 the employed equivalent circuit is reported in Fig. 11b, where Q_{dl} models the not ideal double layer capacitance and R_P accounts for the polarization resistance. For the AZ31 alloys with MnST deposition after $MgSn(OH)_6$ conversion layer two time constants are necessary (EEC in Fig. 11c) to account for the presence of MnST grown on uncoated bare alloy and sealing the empty space between $MgSn(OH)_6$ spheres (see Fig. 8b). Indeed, R_i and Q_i account for the non-ideal capacitance and for the resistance of the manganese stearate layer electrodeposited on uncoated regions beneath and/or among the $MgSn(OH)_6$ spheres, while R_o and Q_o account for the non-ideal capacitance and for the resistance of the outer manganese stearate in direct contact with the electrolyte. It is important to mention that the contribution to the measured impedance of magnesium hydroxystannate is in parallel with that of the MnST layer, but it is negligible due to the insulating character of $MgSn(OH)_6$, that is a quaternary metal hydroxide with a dielectric behaviour and a wide band gap [52,53].

Table 5
Percentage of cells growth from 24 to 48 h.

Sample	Fluorescence at 24h	Fluorescence at 48h	Cells Growth %
CTRL	2440	3111	27,5
AZ31	2186	2279	4,2
AZ31/CC30	2095	1905	−9,0
AZ31/CC30/MnST	2037	2450	20,3

Fig. 12 shows the polarization curves recorded by scanning the potential at 5 mV s^{-1} in DMEM at 37 °C. The cathodic branches of the polarization curves are due to both oxygen reduction and hydrogen evolution, while the anodic current is associated to the metal oxidation. The presence of the coating reduces the current density in the anodic branches and slightly shifts the pitting potential to more positive values. However, for alloys after chemical conversion the shift in the corrosion potential is so high that it is coincident with the pitting potential, thus explaining their very high pitting susceptibility. Moreover, for alloy directly coated by manganese stearate (AZ31/MnST) the corrosion potential and the corresponding corrosion current density are reduced by the layer, but the pitting potential is coincident with that of the bare alloy. This could be also because of the poor adhesion of the coating on the bare alloy. For hydrophobic Mn stearate layer deposited directly on bare AZ31 the coating showed lower mechanical stability than with the conversion coating used as substrate, leading to a lower corrosion resistance. The AZ31/CC30/MnST samples show the best performance in terms of reduction of corrosion current density with a pitting potential far enough from the corrosion potential (>250 mV).

It is crucial to remember that Mg and Mg alloys show a characteristic behaviour known as negative difference effect (NDE), with the consequence that during an anodic polarization over their corrosion potential, dissolution rates increase together with hydrogen evolution rate (HER) [54]. This leads to uncertainty in the evaluation of hydrogen evolution rate from the corrosion current density estimated by fitting polarization curves, and it requires the introduction of a different experimental approach. Different methods have been adopted to evaluate HER, like measuring hydrogen accumulation in closed containers thanks to the weight change in a buoyant system, or by indirect evaluation with pressure sensors and O_2 sensors [55,56]. The method used in this study allows the direct measurement of H_2 concentration, collecting a gas sample directly from the closed container where the metallic sample is corroding, namely DMEM solution at 37 °C in this work. The gas sample is then analysed by a gas chromatograph, providing precise concentration values representative of the atmosphere in the head volume of the container. H_2 concentration values were collected regularly over 168 h, allowing to measure the amount of hydrogen evolved over time. Reporting collected data in *ml* cm^{-2}, and the time in *days*, HER could then be estimated as the slope of the interpolating straight line. Slope values are reported in Fig. 13, where it can be seen that a strong reduction of hydrogen evolution rate with respect to bare AZ31 can be provided by a 60 min chemical conversion coating, but with AZ31/CC30/MnST samples the behaviour is even better since the evolved H_2 cannot be appreciated after 24 h in agreement with the recorded EIS spectra (see Fig. 10) and remains constant under 0.08 ml cm^{-2} $days^{-1}$ up to 168 h of immersion.

3.4. Cytotoxicity tests

Cytotoxicity tests were carried out to evaluate the potential of stannate conversion coating and Mn stearate coating as biomaterial for biomedical applications. Fig. 14 shows the percentage of viable cells grown in each conditioned medium with respect to the control (i.e. cells grown in normal medium). After 24 h, the viability of cells exposed to AZ31-, AZ31/CC30-, and AZ31/CC30/MnST-treated samples was 89.6 %, 85.9 %, and 83.5 %, respectively. All samples exhibited over 70 % viability, indicating non-toxicity after 24 h. At 48 h, the AZ31/CC30/MnST-treated samples maintained a high viability, 78.7 %, confirming their cytocompatibility, whereas lower values were recorded for AZ31 (73.2 %) and AZ31/CC30 (61.2 %).

Additionally, growth rates were calculated by comparing for each sample the value of fluorescence (directly proportional to the number of viable cells) at 24 and 48 h. Results in Table 5 show a 9 % decrease, in terms of viable cells, for cells exposed to AZ31/CC30-medium and a slight increase (4.2 %) of cells treated with AZ31-medium. Interestingly, cells treated with AZ31/CC30/MnST-medium showed a 20.3 % increase, the closest to that observed in the control (27.5 %). Overall, these results not only highlight the cytocompatibility of MnST coated samples, but also suggest a positive effect on cell growth with respect to the bare metal.

4. Conclusions

A double step process, consisting in a first stannate based chemical conversion followed by manganese stearate electrodeposition, was employed in order to slow down the magnesium corrosion rate in DMEM. The hydrophobic coating obtained in the second step was successfully optimized for the stannate based substrate, ensuring a good adhesion and a great improvement in the overall impedance with respect to the bare alloy. The recorded EIS spectra show the absence of inductive loop, suggesting the formation of a compact and protective layer on the AZ31 substrate. The gas chromatography measurements for the direct estimation of H_2 evolution allowed to confirm this result, reaching a hydrogen evolution rate of 0.08 ml cm^{-2} $days^{-1}$ even after 168 h. Furthermore, cytocompatibility of the coating was confirmed by the vitality test, maintaining acceptable values even after 48 h.

Funding

M.S. and F.D.F. acknowledge the European Union (NextGeneration EU), for the support through the MUR-PNRR project SAMOTHRACE.

V.V. acknowledges the European Union (NextGeneration EU), for funding PhD Scholarship.

Declaration of competing interest

The authors declare that they have no known competing financial interests or personal relationships that could have appeared to influence the work reported in this paper.

References

[1] M. He, L. Chen, M. Yin, S. Xu, Z. Liang, Review on magnesium and magnesium-based alloys as biomaterials for bone immobilization, J. Mater. Res. Technol. 23 (2023) 4396–4419, https://doi.org/10.1016/j.jmrt.2023.02.037.
[2] H. Dong, F. Lin, A.R. Boccaccini, S. Virtanen, Corrosion behavior of biodegradable metals in two different simulated physiological solutions: comparison of Mg, Zn and Fe, Corros. Sci. 182 (2021), https://doi.org/10.1016/j.corsci.2021.109278.
[3] T. Zhang, W. Wang, J. Liu, L. Wang, Y. Tang, K. Wang, A review on magnesium alloys for biomedical applications, Front. Bioeng. Biotechnol. 10 (2022), https://doi.org/10.3389/fbioe.2022.953344.
[4] D. Bairagi, S. Mandal, A comprehensive review on biocompatible Mg-based alloys as temporary orthopaedic implants: current status, challenges, and future prospects, J. Magn. Alloys 10 (2022) 627–669, https://doi.org/10.1016/j.jma.2021.09.005.
[5] D. Li, D. Zhang, Q. Yuan, L. Liu, H. Li, L. Xiong, X. Guo, Y. Yan, K. Yu, Y. Dai, T. Xiao, Y. Li, C. Wen, *In vitro* and *in vivo* assessment of the effect of biodegradable magnesium alloys on osteogenesis, Acta Biomater. 141 (2022) 454–465, https://doi.org/10.1016/j.actbio.2021.12.032.
[6] F. Xing, S. Li, D. Yin, J. Xie, P.M. Rommens, Z. Xiang, M. Liu, U. Ritz, Recent progress in Mg-based alloys as a novel bioabsorbable biomaterials for orthopedic applications, J. Magn. Alloys 10 (2022) 1428–1456, https://doi.org/10.1016/j.jma.2022.02.013.
[7] F.Z. Akbarzadeh, M. Sarraf, E.R. Ghomi, V.V. Kumar, M. Salehi, S. Ramakrishna, S. Bae, A state-of-the-art review on recent advances in the fabrication and characteristics of magnesium-based alloys in biomedical applications, J. Magn. Alloys 12 (2024) 2569–2594, https://doi.org/10.1016/j.jma.2024.06.015.
[8] N.G. Sommer, D. Hirzberger, L. Paar, L. Berger, H. Ćwieka, U.Y. Schwarze, V. Herber, B. Okutan, A.J. Bodey, R. Willumeit-Römer, B. Zeller-Plumhoff, J. F. Löffler, A.M. Weinberg, Implant degradation of low-alloyed Mg-Zn-Ca in osteoporotic, old and juvenile rats, Acta Biomater. 147 (2022) 427–438, https://doi.org/10.1016/j.actbio.2022.05.041.
[9] D.H. Cho, T. Avey, K.H. Nam, D. Dean, A.A. Luo, In vitro and in vivo assessment of squeeze-cast Mg-Zn-Ca-Mn alloys for biomedical applications, Acta Biomater. 150 (2022) 442–455, https://doi.org/10.1016/j.actbio.2022.07.040.
[10] J. Wu, X. Cheng, J. Wu, J. Chen, X. Pei, The development of magnesium-based biomaterials in bone tissue engineering: a review, J. Biomed. Mater. Res. B Appl. Biomater. 112 (2024), https://doi.org/10.1002/jbm.b.35326.
[11] M.A. Osipenko, D.S. Kharytonau, A.A. Kasach, J. Ryl, J. Adamiec, I.I. Kurilo, Inhibitive effect of sodium molybdate on corrosion of AZ31 magnesium alloy in

chloride solutions, Electrochim. Acta 414 (2022), https://doi.org/10.1016/j.electacta.2022.140175.
[12] S.V.S. Prasad, S.B. Prasad, K. Verma, R.K. Mishra, V. Kumar, S. Singh, The role and significance of magnesium in modern day research-a review, J. Magn. Alloys 10 (2022) 1–61, https://doi.org/10.1016/j.jma.2021.05.012.
[13] H.W. Hassan, V. Grasso, O. Korostynska, H. Khan, J. Jose, P. Mirtaheri, An overview of assessment tools for determination of biological Magnesium implant degradation, Med. Eng. Phys. 93 (2021) 49–58, https://doi.org/10.1016/j.medengphy.2021.05.016.
[14] H.W. Hassan, M. Rahmati, A. Barrantes, H.J. Haugen, P. Mirtaheri, *In vitro* monitoring of magnesium-based implants degradation by surface analysis and optical spectroscopy, Int. J. Mol. Sci. 23 (2022) 6099, https://doi.org/10.3390/ijms23116099.
[15] P. Tong, Y. Sheng, R. Hou, M. Iqbal, L. Chen, J. Li, Recent progress on coatings of biomedical magnesium alloy, Smart. Mater. Med. 3 (2022) 104–116, https://doi.org/10.1016/j.smaim.2021.12.007.
[16] M. Echeverry-Rendón, L.F. Berrio, S.M. Robledo, J.A. Calderón, J.G. Castaño, F. Echeverría, Corrosion resistance and biological properties of pure magnesium modified by PEO in alkaline phosphate solutions, Corros. Mater. Degradat. 4 (2023) 196–211, https://doi.org/10.3390/cmd4020012.
[17] D. Chen, D. Mei, Y. Li, L. Chen, H. Wang, W. Huang, L. Wang, S. Zhu, S. Guan, Protective nature of cerium-based oxides coating against Mg corrosion in Hanks' balanced salt solution, Corros. Sci. 219 (2023) 111255, https://doi.org/10.1016/j.corsci.2023.111255.
[18] S. Seetharaman, D. Sankaranarayanan, M. Gupta, Magnesium-based temporary implants: potential, current status, applications, and challenges, J. Funct. Biomater. 14 (2023) 324, https://doi.org/10.3390/jfb14060324.
[19] L. Wei, Z. Gao, Recent research advances on corrosion mechanism and protection, and novel coating materials of magnesium alloys: a review, RSC. Adv. 13 (2023) 8427–8463, https://doi.org/10.1039/D2RA07829E.
[20] G. Di Egidio, L. Tonelli, A. Morri, I. Boromei, P. Shashkov, C. Martini, Influence of anodizing by electro-chemical oxidation on fatigue and wear resistance of the EV31A-T6 cast magnesium alloy, Coatings 13 (2022) 62, https://doi.org/10.3390/coatings13010062.
[21] L. Govind Sanjeev Kumar, D. Thirumalaikumarasamy, K. Karthikeyan, M. Mathanbabu, M. Ashokkumar, C.S. Ramachandran, An overview of recent trends and challenges of post treatments on magnesium alloys, Mater. Today Proc. 78 (2023) 700–707, https://doi.org/10.1016/j.matpr.2023.01.071.
[22] M. Rahmati, K. Raeissi, M.R. Toroghinejad, A. Hakimizad, M. Santamaria, Corrosion and wear resistance of coatings produced on AZ31 Mg alloy by plasma electrolytic oxidation in silicate-based K2TiF6 containing solution: effect of waveform, J. Magn. Alloys 10 (2022) 2574–2587, https://doi.org/10.1016/j.jma.2021.07.026.
[23] A. Zaffora, F. Di Franco, D. Virtù, F. Carfì Pavia, G. Ghersi, S. Virtanen, M. Santamaria, Tuning of the Mg alloy AZ31 anodizing process for biodegradable implants, ACS. Appl. Mater. Interfaces. 13 (2021) 12866–12876, https://doi.org/10.1021/acsami.0c22933.
[24] M. Nasr Azadani, A. Zahedi, O.K. Bowoto, B.I. Oladapo, A review of current challenges and prospects of magnesium and its alloy for bone implant applications, Prog. Biomater. 11 (2022) 1–26, https://doi.org/10.1007/s40204-022-00182-x.
[25] H. Mei, H. Song, K. Feng, Y. Chen, H. Yan, C. Luo, D. Liu, H. Guan, C. Luc, Z. Hu, Corrosion protection of folic acid and lauric acid modified films prepared by anodic oxidation on WE43 magnesium alloys, Appl. Surf. Sci. 638 (2023) 158014, https://doi.org/10.1016/j.apsusc.2023.158014.
[26] P. Zhang, Y. Zuo, G. Nie, The enhanced properties of anodic films on AZ91D magnesium alloy by addition of oxide nanoparticles, J. Alloys. Compd. 834 (2020) 155041, https://doi.org/10.1016/j.jallcom.2020.155041.
[27] M. L, S. Kar, N. B, S.S. Dhilip Kumar, M. Nagai, T.S. Santra, Formation of nanostructures on magnesium alloy by anodization for potential biomedical applications, Mater. Today Commun. 25 (2020) 101403, https://doi.org/10.1016/j.mtcomm.2020.101403.
[28] J. Moreno, J.L. Merlo, A.C. Renno, J. Canizo, F.J. Buchelly, J.I. Pastore, M. R. Katunar, S. Cere, In vitro characterization of anodized magnesium alloy as a potential biodegradable material for biomedical applications, Electrochim. Acta 437 (2023) 141463, https://doi.org/10.1016/j.electacta.2022.141463.
[29] J. Jiao, Y. Gu, X. Ding, J. Zhang, Y. Lian, P. Gao, X. Zhang, S. Han, K. Zheng, F. Pan, Effect of different metal-reinforcement phases on PEO discharge and coating growth behavior of AZ91 Mg-matrix composites, J. Magn. Alloys (2025), https://doi.org/10.1016/j.jma.2025.01.008.
[30] N.A. Johari, J. Alias, A. Zanurin, N.S. Mohamed, N.A. Alang, M.Z.M. Zain, Anti-corrosive coatings of magnesium: a review, Mater. Today Proc. 48 (2022) 1842–1848, https://doi.org/10.1016/j.matpr.2021.09.192.
[31] E. Mysliu, K. Sletteberg Storli, H.M. Skogøy, S. Kubowicz, I.H. Svenum, O. Lunder, A. Erbe, Effect of Cu2+ on deposition mechanism and structure of ZrO2-based conversion coatings on AA6060 aluminium alloys and their susceptibility to filiform corrosion, Electrochim. Acta 477 (2024) 143805, https://doi.org/10.1016/j.electacta.2024.143805.
[32] X. Xue, C. Liang, D. Wang, F. Peng, The research progress of self-healing coatings for magnesium/magnesium alloy, J. Alloys. Compd. 960 (2023) 170710, https://doi.org/10.1016/j.jallcom.2023.170710.
[33] N. Singh, U. Batra, K. Kumar, N. Ahuja, A. Mahapatro, Progress in bioactive surface coatings on biodegradable Mg alloys: a critical review towards clinical translation, Bioact. Mater. 19 (2023) 717–757, https://doi.org/10.1016/j.bioactmat.2022.05.009.
[34] R. Xu, Y. Li, B. Fan, Y. Weng, Y. Zhou, F. Yan, One-step preparation of molybdate-stannate-tungstate composite conversion coating on magnesium alloy AZ91D and its microstructure and corrosion resistance, Int. J. Electrochem. Sci. 18 (2023) 100398, https://doi.org/10.1016/j.ijoes.2023.100398.
[35] D. Zhang, F. Peng, X. Liu, Protection of magnesium alloys: from physical barrier coating to smart self-healing coating, J. Alloys. Compd. 853 (2021) 157010, https://doi.org/10.1016/j.jallcom.2020.157010.
[36] A.S. Hamdy, D.P. Butt, Novel smart stannate based coatings of self-healing functionality for AZ91D magnesium alloy, Electrochim. Acta 97 (2013) 296–303, https://doi.org/10.1016/j.electacta.2013.02.108.
[37] H.H. Elsentriecy, K. Azumi, H. Konno, Improvement in stannate chemical conversion coatings on AZ91 D magnesium alloy using the potentiostatic technique, Electrochim. Acta 53 (2007) 1006–1012, https://doi.org/10.1016/j.electacta.2007.08.015.
[38] F. Di Franco, A. Zaffora, P. Vassallo, M. Santamaria, Double step electrochemical process for the deposition of superhydrophobic coatings for enhanced corrosion resistance, J. Electrochem. Soc. 168 (2021), https://doi.org/10.1149/1945-7111/ac29df.
[39] T.P. Rasitha, N.G. Krishna, B. Anandkumari, S.C. Vanithakumari, J. Philip, A comprehensive review on anticorrosive/antifouling superhydrophobic coatings: fabrication, assessment, applications, challenges and future perspectives, Adv. Colloid. Interface Sci. 324 (2024) 103090, https://doi.org/10.1016/j.cis.2024.103090.
[40] L. Zhang, X. Liu, J. Yan, Z. Li, S. Huang, Y. Weng, J. Li, C. Yuan, P. Han, S. Ye, X. Zhang, Preparation of superhydrophobic coating with anti-corrosion and anti-fouling properties on the surface of low manganese steel by electrodeposition, Surf. Coat. Technol. 460 (2023) 129412, https://doi.org/10.1016/j.surfcoat.2023.129412.
[41] J. Tian, J. Bao, L. Li, J. Sha, W. Duan, M. Qiao, J. Cui, Z. Zhang, Facile fabrication of superhydrophobic coatings with superior corrosion resistance on LA103Z alloy by one-step electrochemical synthesis, Surf. Coat. Technol. 452 (2023) 129090, https://doi.org/10.1016/j.surfcoat.2022.129090.
[42] G.L. Song, A. Atrens, Recently deepened insights regarding Mg corrosion and advanced engineering applications of Mg alloys, J. Magnes. Alloys 11 (2023) 3948–3991, https://doi.org/10.1016/j.jma.2023.08.012.
[43] C.Q. Li, D.K. Xu, Z.R. Zhang, E.H. Han, Influence of the lithium content on the negative difference effect of Mg-Li alloys, J. Mater. Sci. Technol. 57 (2020) 138–145, https://doi.org/10.1016/j.jmst.2020.03.046.
[44] J. Zhang, J. Miao, N. Balasubramani, D.H. Cho, T. Avey, C.Y. Chang, A.A. Luo, Magnesium research and applications: past, present and future, J. Magnes. Alloys 11 (2023) 3867–3895, https://doi.org/10.1016/j.jma.2023.11.007.
[45] R.B. Heimann, Magnesium alloys for biomedical application: advanced corrosion control through surface coating, Surf. Coat. Technol. 405 (2021) 126521, https://doi.org/10.1016/j.surfcoat.2020.126521.
[46] T.W. Cain, I. Gonzalez-Afanador, N. Birbilis, J.R. Scully, The role of surface films and dissolution products on the negative difference effect for magnesium: comparison of Cl^- versus Cl^- free solutions, J. Electrochem. Soc. 164 (2017) C300–C311, https://doi.org/10.1149/2.1371706jes.
[47] D. Pupillo, M.P. Bruns, L.H. Prado, F. Di Franco, D. Böhringer, A. Mazare, W. H. Goldmann, S. Virtanen, M. Santamaria, A.B. Tesler, Corrosion resistance of biodegradable zinc surfaces enhanced by UV-grafted polydimethylsiloxane coating, ACS. Biomater. Sci. Eng. 10 (2024) 4891–4900, https://doi.org/10.1021/acsbiomaterials.4c00503.
[48] M.S. Hossain, T. Ha, C. Song, V. Panov, C. Seunghak, K.K. Yun, Effects of aluminum and barium stearates on hydrophobic material production, J. Build. Eng. 98 (2024), https://doi.org/10.1016/j.jobe.2024.111152.
[49] Y. Li, X. Tian, Y. Wang, Q. Yang, Y. Diao, B. Zhang, D. Yang, In situ construction of a MgSn(OH)6 perovskite/SnO2 type-II heterojunction: a highly efficient photocatalyst towards photodegradation of tetracycline, Nanomaterials 10 (2020), https://doi.org/10.3390/nano10010053.
[50] V. Verro, F. Di Franco, A. Zaffora, M. Santamaria, Enhancing corrosion resistance of anodized AA7075 alloys by electrodeposition of superhydrophobic coatings, Colloids. Surf. A Physicochem. Eng. Asp. 675 (2023), https://doi.org/10.1016/j.colsurfa.2023.132040.
[51] M. Curioni, L. Salamone, F. Scenini, M. Santamaria, M. Di Natale, A mathematical description accounting for the superfluous hydrogen evolution and the inductive behaviour observed during electrochemical measurements on magnesium, Electrochim. Acta 274 (2018) 343–352, https://doi.org/10.1016/j.electacta.2018.04.116.
[52] P.X. Gao, P. Shimpi, H. Gao, C. Liu, Y. Guo, W. Cai, K.T. Liao, G. Wrobel, Z. Zhang, Z. Ren, H.J. Lin, Hierarchical assembly of multifunctional oxide-based composite nanostructures for energy and environmental applications, Int. J. Mol. Sci. 13 (2012) 7393–7423, https://doi.org/10.3390/ijms13067393.
[53] L. Anicai, R. Masi, M. Santamaria, F. Di Quarto, A photoelectrochemical investigation of conversion coatings on Mg substrates, Corros. Sci. 47 (2005) 2883–2900, https://doi.org/10.1016/j.corsci.2005.05.033.
[54] A.Z. Benbouzid, M.P. Gomes, I. Costa, O. Gharbi, N. Pébère, J.L. Rossi, M.T.T. Tran, B. Tribollet, M. Turmine, V. Vivier, A new look on the corrosion mechanism of magnesium: an EIS investigation at different pH, Corros. Sci. 205 (2022), https://doi.org/10.1016/j.corsci.2022.110463.
[55] M. Strebl, M. Bruns, S. Virtanen, Editors' choice—respirometric in situ methods for real-time monitoring of corrosion rates: part I. Atmospheric corrosion, J. Electrochem. Soc. 167 (2020) 021510, https://doi.org/10.1149/1945-7111/ab6c61.
[56] B. Dou, X. Li, J. Han, K. Ogle, Operando kinetics of hydrogen evolution and elemental dissolution I: the dissolution of galvanized steel in hydrochloric acid, Corros. Sci. 214 (2023), https://doi.org/10.1016/j.corsci.2023.111007.